OPEN ACCESS
Journal of Innovative Optical Health Sciences
2150018 (9 pages)

DOI: 10.1142/S1793545821500188

A comparative study on machine learning-based classification to find photothrombotic lesion in histological rabbit brain images

Sang Hee Jo*, Yoonhee Kim†, Yoon Bum Lee‡,
Sung Suk Oh†,§ and Jong-ryul Choi†,¶
*School of Biomedical Engineering
Daegu Catholic University (DCU)
Gyeongsan, 38430, Republic of Korea
†Medical Device Development Center
Daegu-Gyeongbuk Medical Innovation
Foundation (DGMIF)
Daegu 41061, Republic of Korea
‡Laboratory Animal Center
Daegu-Gyeongbuk Medical Innovation
Foundation (DGMIF), Daegu 41061, Republic of Korea
§ssoh@dgmif.re.kr
¶jongryul32@dgmif.re.kr

Received 25 March 2021
Accepted 1 June 2021
Published 2 July 2021

Recently, research has been conducted to assist in the processing and analysis of histopathological images using machine learning algorithms. In this study, we established machine learning-based algorithms to detect photothrombotic lesions in histological images of photothrombosis-induced rabbit brains. Six machine learning-based algorithms for binary classification were applied, and the accuracies were compared to classify normal tissues and photothrombotic lesions. The lesion classification model consisting of a 3-layered neural network with a rectified linear unit (ReLU) activation function, Xavier initialization, and Adam optimization using datasets with a unit size of 128×128 pixels yielded the highest accuracy (0.975). In the validation using the tested histological images, it was confirmed that the model could identify regions where brain damage occurred due to photochemical ischemic stroke. Through the development of machine learning-based photothrombotic lesion classification models and performance comparisons, we confirmed that machine learning algorithms have the potential to be utilized in histopathology and various medical diagnostic techniques.

Keywords: Machine learning; histopathological images; photothrombotic lesion; rabbit brain; binary classification; logistic regression; multi-layer neural networks.

§,¶Corresponding authors.

1. Introduction

Machine learning is an algorithmic technique that solves a particular problem through a learned experience, similar to a human.[1] Specifically, repeated learning from well-organized data results in algorithms exhibiting high performance in conducting particular tasks, and building and applying them are the main tasks performed in machine learning. Machine learning has been utilized in predicting results using trained data, complex, multi-dimensional, and large-scale data classification, and pattern recognition from images.[2–7]

Machine learning algorithms with high performance and accuracy based on the accumulated dataset have also been applied to research in the fields of biology and medical technologies. For instance, a machine learning algorithm was developed to predict the function of non-coded DNA by estimating transcription factor binding sites.[8] Several research groups have investigated machine learning-based high-performance cell/cellular component classification techniques in microscopic images.[9,10] Research on machine learning software that improves the resolution of microscopic images by training low-resolution and high-resolution images as datasets has also been actively conducted.[11–13] In the medical field, research has been conducted to classify lesions or extract exclusive medical information from medical images, such as computed tomography (CT) and magnetic resonance imaging (MRI) using machine learning-based image processing.[14,15] In particular, in accordance with the development of machine learning-based image processing techniques for microscopic and medical images, research to assist in the diagnosis of disease or classify lesions in histopathological images using machine learning has been actively conducted.[16–18] For example, Zeng and Zhang introduced high-performance detection of carcinoma in histological images using a machine learning algorithm programmed by Google AutoML.[19] Xia *et al.* developed a deep learning algorithm for tumor classification using histological images.[20]

In this study, a machine learning-based classification model was programmed to detect photothrombotic lesions in histological images of a rabbit brain. Training and test datasets were extracted from the histological images of hematoxylin and eosin (H&E) stained tissue slices from the brains of photothrombosis-induced rabbits. Based on the datasets, a machine learning algorithm to distinguish photothrombotic lesions from the brain tissue images was established. We constructed training and test datasets with two unit sizes of 64×64 pixels and 128×128 pixels. The machine learning-based classification model was applied to both the datasets, and the algorithm trained using images of a unit size of 128×128 pixels showed higher accuracy. In addition, we applied six machine learning-based classification models that performed binary classification on the training and test datasets, and confirmed that the 3-layered neural network with the rectified linear unit (ReLU) activation function, Xavier initialization, and adaptive movement estimation (Adam) optimization yielded the highest accuracy (0.975) in the dataset with a unit size of 128×128 pixels. The results of the development of lesion classification algorithms and accuracy comparison with conditional changes are expected to be an important milestone in the application and practicality of machine learning techniques for histopathologic image analysis.

2. Materials and Methods

2.1. *Sample preparation – from photothrombosis induction in a rabbit brain to brain image acquisition*

The development of a photothrombosis investigation system and the establishment of a photochemical ischemic stroke rabbit model using the system were presented in detail in a previous study.[21] All experimental procedures were approved by the Animal Experiment Ethics Committee of Daegu–Gyeongbuk Medical Innovation Foundation (Approval number: DGMIF-20061702-00). A brief description of the overall photothrombosis induction process is as follows: four 12-week-old, male New Zealand White rabbits obtained from Samtaco (Osan, Republic of Korea) were used in this study. The rabbits were anesthetized by an intramuscular (IM) injection of Zoletil (Zoletil 50 injection, Virbac Korea, Seoul, Republic of Korea) with a concentration of 15 mg/kg and Rompun (Rompun injection, Bayer Korea, Seoul, Republic of Korea) with a concentration of 10 mg/kg before the operation. Surgery was performed to remove the hair and scalp to reveal the skull. After exposure of the skull, Rose Bengal diluted to 10 mg/mL was injected through

an ear vein with a concentration of 80 mg/kg, and LASER light (125 mW) was irradiated on a targeted region in the rabbit brain for 30 min. To minimize pain, additional anesthesia during laser irradiation was administered through the respiratory system using 1.5% isoflurane (Ifran Liq, Hana Pharm Co., Ltd., Seoul, Republic of Korea). After the induction of photochemical thrombosis, the wound was sutured using 4/0 polydioxanone and 3/0 nylon sutures.

T2-weighted MRI was performed once every 24 h to determine whether and where photothrombotic brain lesions occurred. After 72 h, the rabbit brain was extracted and brain damage was cross-validated using 2,3,5-triphenyltetrazolium chloride (TTC) staining. After the procedures, brain sections were fixed in 4% paraformaldehyde (M1176, Biostem, Suwon, Republic of Korea) and embedded in paraffin. The paraffin blocks of brain sections were cut to 4 μm thickness using a microtome. To visualize the photothrombotic lesion area and tissue properties, each section was stained with H&E stain kit (H3502, Vector Laboratories, Inc., Burlingame, CA, United States) and bright-field images of H&E stained brain sections were obtained using a slide scanning microscope (Zeiss Axio Scan.Z1, Carl Zeiss, Jena, Germany).

2.2. *Establishment of datasets and lesion classification algorithm using machine learning*

As a first step in the establishment of training datasets, we extracted images with a size of 6,400 × 6,400 pixels from ipsilesional and contralesional areas in three slide images of the rabbit brain. They were then divided into unit sizes of 64 × 64 (overlap ratio: 0%) and 128 × 128 pixels (overlap ratio: 50 %). As a test dataset, we employed four images (12,800 × 3,200 pixels) containing normal tissue and photothrombotic lesions from unused rabbit brain images in training datasets. Each test image was divided into the unit sizes set in the training dataset and evaluated by machine learning classification algorithms to determine whether it is a normal tissue or photothrombotic lesion. Acquisitions and segmentations of images in datasets were performed using Zeiss ZEN 3.1 (Blue edition).

Preprocessing was performed to convert the intensities of each training and test image dataset into the array form. Each image of the unit size was converted to an 8-bit intensity value of 32 × 32 pixels (= 1,024 pixels). Thus, the size of the training dataset, with 60,000 images for normal tissue and photothrombotic lesions extracted from three brain slide images, consists of a matrix with a size of 60,000 × 1,024. Each test image, divided into a unit size, is similarly composed of an array with a size of 1 × 1,024. This preprocessing and dataset configuration was performed using GNU Octave and Python. A schematic of the dataset preparation is shown in Fig. 1.

In this study, six machine learning-based algorithms were applied for binary classification and the differences in accuracy were compared: (1) logistic regression with sigmoidal activation function and gradient descent optimization; (2) 3-layered neural network with sigmoid activation function and gradient descent optimization; (3) 3-layered neural network with ReLU activation function, Xavier initialization, and gradient descent optimization; (4) 3-layered neural network with ReLU activation function, He normal initialization, and gradient descent optimization; (5) 3-layered neural network with ReLU activation function, Xavier initialization, and Adam optimization; and (6) 3-layered neural network with ReLU activation function, He normal initialization, and Adam optimization (as shown in Fig. 2). In the 3-layered neural network, each hidden layer consisted of 10 neurons. Each algorithm used in this study is programmed to input, compute and classify dataset from brain images, which were segmented to determined unit sizes, based on logistic regression.[22–24] In addition, a sigmoid function was used to acquire the final normal/photothrombotic lesion discrimination in the algorithm with the ReLU activation function in the hidden layers.

Weight initialization was applied to improve the learning efficiency and ensure that there were no inoperative neurons in the hidden layer. We confirmed that a 3-layered neural network with a ReLU activation function and no initialization did not learn in the direction of reducing the cost of learning on the dataset in this study. Among the weight initialization techniques discovered by previous studies,[25,26] two techniques, Xavier initialization and He normal initialization, were applied. In Xavier initialization, an initial optimized weight is defined as follows:

$$\mathbf{W} \sim \mathcal{U}\left(-\sqrt{\frac{6}{n_{\text{in}} + n_{\text{out}}}}, +\sqrt{\frac{6}{n_{\text{in}} + n_{\text{out}}}}\right).$$

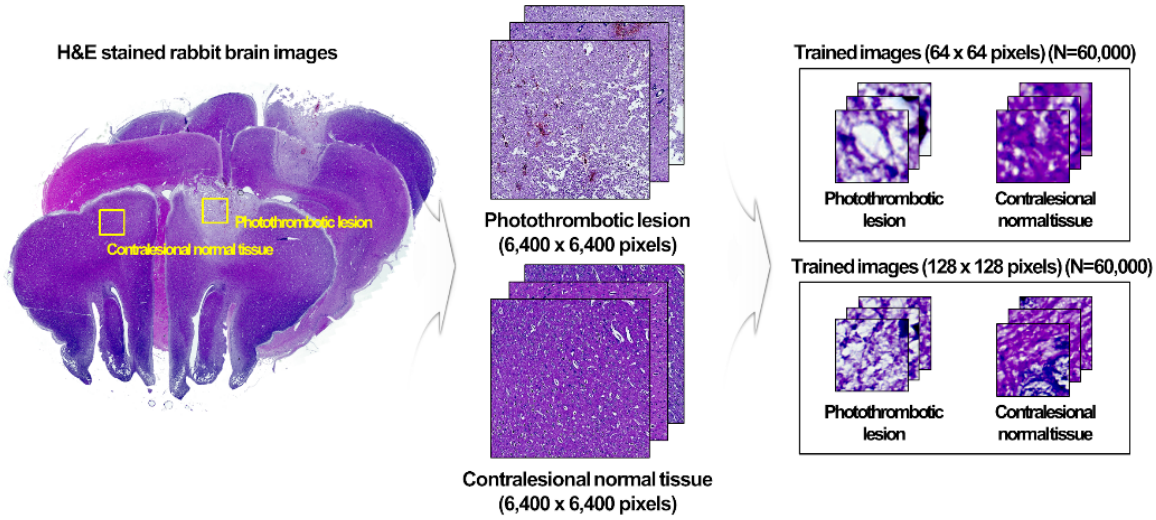

Fig. 1. Schematic of training dataset preparation from entire slide images of H&E stained rabbit brain with a photothrombotic lesion. First, we extracted images with a unit size of 6,400 × 6,400 pixels from ipsilesional and contralesional areas in the brain image. They were then divided into unit sizes of 64 × 64 (overlap ratio = 0%) and 128 × 128 pixels (overlap ratio = 50%). In addition, we segmented four test images with a size of 12,800 × 3,200 pixels in the same manner to confirm the possibility of identifying photothrombotic lesions.

where n_{in} and n_{out} are the number of nodes in the front and next layers, respectively, and $\mathcal{U}()$ denotes a uniform distribution function. In addition, in He normal initialization, an initial optimized weight is defined as follows:

$$\mathbf{W} \sim \mathcal{N}(0, \boldsymbol{Var}(\mathbf{W})),$$
$$\boldsymbol{Var}(\mathbf{W}) = \sqrt{\frac{2}{n_{\text{in}}}},$$

where $\mathcal{N}()$ denotes a normal distribution function.

The neural network advances in the direction of reducing cost (loss) by learning and improving the accuracy of the machine learning-based classification model built through it. A basic method of cost reduction is gradient descent optimization, which determines weights and biases corresponding to the minimum cost by changing input weights and biases with a constant size corresponding to the product of the step size and the slope of the cost function. The gradient descent optimizer is expressed mathematically as follows:

$$(\mathbf{W}, \mathbf{b}) = (\mathbf{W}, \mathbf{b}) - \eta \nabla_{\mathbf{W},\mathbf{b}} \boldsymbol{C}(\mathbf{W}, \mathbf{b}),$$

where $\mathbf{W}$ and $\mathbf{b}$ denote the weights and biases in the machine learning-based classification model, respectively, and η is a step size. In this study, we selected 0.01 as a step size to find the minimum cost. $\boldsymbol{C}(\mathbf{W}, \mathbf{b})$ is the cost function and $\nabla_{\mathbf{W},\mathbf{b}}$ denotes the gradient. The gradient descent optimization is divided into a batch gradient descent optimization, which learns over the entire dataset and extracts the cost and accuracy at each iteration, and stochastic gradient descent optimization, which randomly extracts and learns a part of the dataset at each iteration. In this study, we applied the batch gradient descent optimization. In addition, we employed Adam optimization,[27,28] which yields higher performance than the gradient descent optimization, to find an optimized hypothesis for minimizing cost. The Adam optimizer computes and stores the means of gradients (m_t) and the square of gradients (v_t), and calculates the corrected expectation using them and the exponential decay rates (β_1 and β_2) of the first- and second-order moment estimates. It then uses this expectation to move hypotheses on the cost function and perform optimization to find the hypothesis with the lowest cost. The Adam optimizer is expressed mathematically as follows:

$$(\mathbf{W}, \mathbf{b}) = (\mathbf{W}, \mathbf{b}) - \frac{\eta}{\sqrt{\hat{v_t} + \epsilon}} \hat{m_t},$$

where

$$\hat{m_t} = \frac{\beta_1 m_{t-1} + (1 - \beta_1) \nabla_{\mathbf{W},\mathbf{b}} \boldsymbol{C}(\mathbf{W}, \mathbf{b})}{1 - \beta_1^t} \quad \text{and}$$
$$\hat{v_t} = \frac{\beta_2 v_{t-1} + (1 - \beta_2)(\nabla_{\mathbf{W},\mathbf{b}} \boldsymbol{C}(\mathbf{W}, \mathbf{b}))^2}{1 - \beta_2^t}.$$

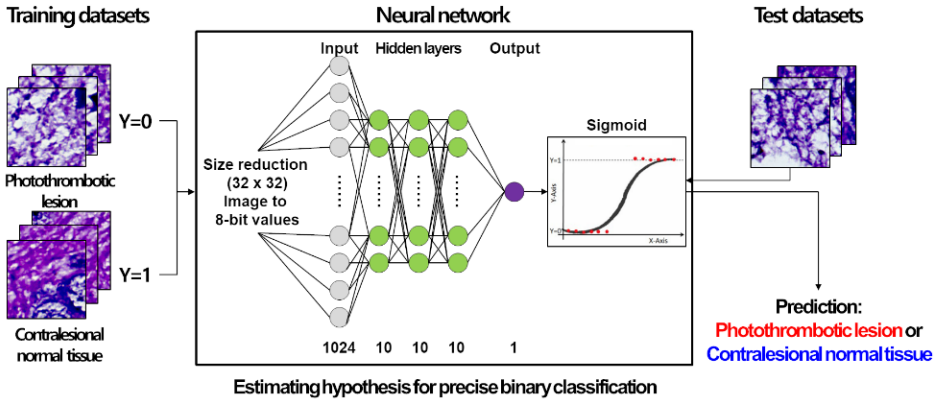

Model number	Hidden layers	Activation function in hidden layers	Initialization	Optimization	Accuracy (500 iterations)		Accuracy (10,000 iterations)	
					64×64	128×128	64×64	128×128
1	X	-	-	Gradient descent optimization	0.490	0.502	0.926	0.956
2	O	Sigmoid	-	Gradient descent optimization	0.909	0.828	0.928	0.962
3	O	Relu	Xavier	Gradient descent optimization	0.918	0.948	0.937	0.965
4	O	Relu	He normal	Gradient descent optimization	0.921	0.943	0.936	0.968
5	O	Relu	Xavier	Adam optimization	0.929	0.958	0.930	0.975
6	O	Relu	He normal	Adam optimization	0.924	0.964	0.500	0.500

Fig. 2. Schematic of machine learning-based algorithms for a binary classification of photothrombotic lesion and normal tissue. We applied six algorithms: (1) Logistic regression with sigmoidal activation function and gradient descent optimization; (2) 3-layered neural network with sigmoid activation function and gradient descent optimization; (3) 3-layered neural network with ReLU activation function, Xavier initialization, and gradient descent optimization; (4) 3-layered neural network with ReLU activation function, He normal initialization, and gradient descent optimization; (5) 3-layered neural network with ReLU activation function, Xavier initialization, and Adam optimization; and (6) 3-layered neural network with ReLU activation function, He normal initialization, and Adam optimization. The hidden layers consisted of a matrix with node numbers of input and output as (1024, 10), (10, 10), and (10, 10), respectively. In addition, the sigmoid function was employed as a function to output the final decision in binary form (0 (photothrombotic lesion) and 1 (normal tissue)). Using the test dataset, classification accuracies of each algorithm with 500 and 10,000 iterations were determined as described in the right side of the table.

ϵ denotes a very small value ($\sim 10^{-8}$) to prevent $\hat{m}_t$ from being divided by zero. To establish the overall classification model, we applied Python version 3.7 embedded in Anaconda and implemented a machine learning-based model using TensorFlow and Keras. Postprocessing of the outputs and image reconstruction were performed using GNU Octave.

3. Results and Discussion

3.1. *Comparative study on unit sizes*

To explore the unit size to provide sufficient spatial resolution for identifying photothrombotic damaged areas in H&E stained rabbit brain images with high accuracy, we compared the accuracies of machine learning-based classification models trained with datasets consisting of segmented images with a unit size of 64×64 and 128×128 pixels, as shown in Fig. 3. As shown in Figs. 3(a) and 3(b), the accuracy converges on all the machine learning classification models except Model 6 (3-layered neural network with ReLU activation function, He normal initialization, and Adam optimization) when sufficient iterations ($N_{\text{Iteration}} = 10{,}000$) were conducted. In the accuracy comparison of the 1-layer logistic regression-based classification model (Model 1) with differences in the unit size, the accuracy of the classifier trained on datasets with a unit size of 64×64 pixels is 0.926 ($= 92.6\%$), and the accuracy of the classifier trained on datasets with a unit size of

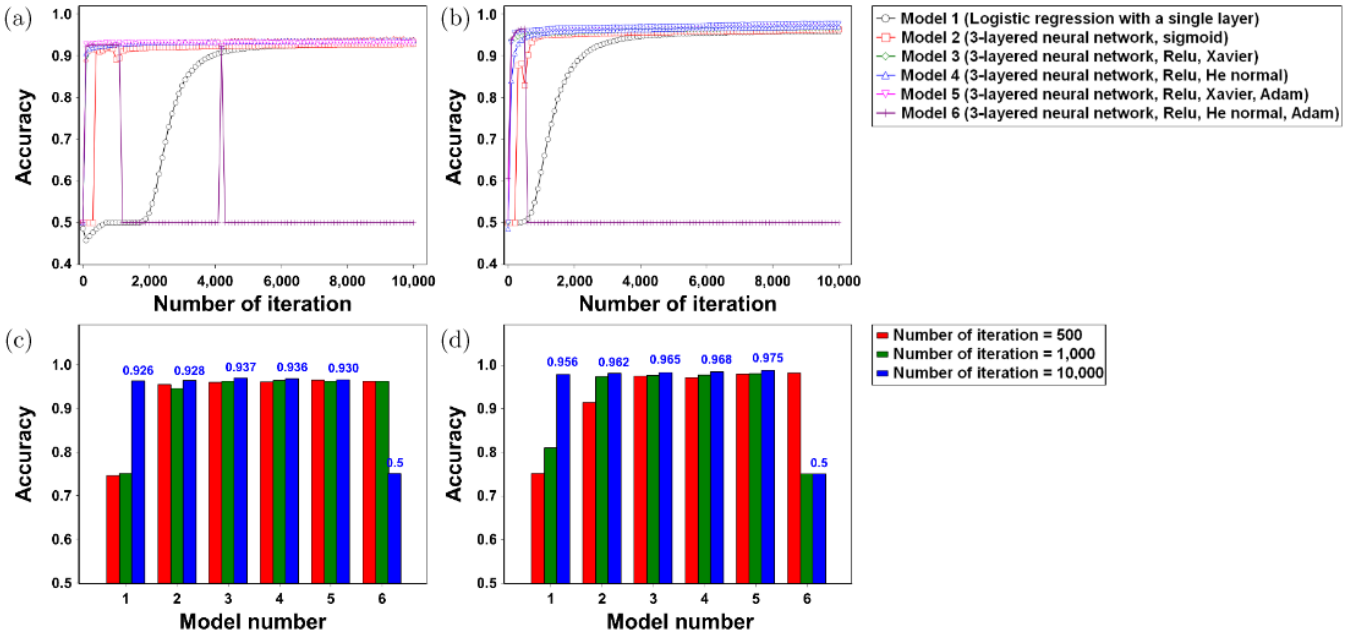

Fig. 3. Plots of accuracy according to the number of iterations ($N_{\text{Iteration}}$) in six machine learning-based lesion classification models trained on the dataset with unit sizes of (a) 64×64 pixels and (b) 128×128 pixels. Bar graphs comparing accuracies according to the machine learning-based models trained on the dataset with unit sizes of (c) 64×64 pixels and (d) 128×128 pixels, with $N_{\text{Iteration}} = 500$, 1,000, and 10,000.

128×128 pixels is 0.956 (= 95.6%), as shown in Figs. 3(c) and 3(d). The mean of the differences in accuracy of the five classification models, excluding Model 6, on the unit size of images in the datasets is 0.0338 (= 3.38%). The results confirm that datasets with a unit size of 128×128 pixels can provide higher accuracy in classifying photothrombotic lesions.

3.2. *Comparative study on machine learning-based photothrombotic lesion classification models*

As described in Fig. 3, changes in accuracy with the progression of iterations in the six machine learning-based classification models were estimated, and the accuracy of each model for $N_{\text{Iteration}} = 500$, 1,000, and 10,000 was compared. Generally, a neural network-based lesion classification model with three hidden layers can be optimized faster at fewer $N_{\text{Iteration}}$ than a lesion classification model with a single layer and no hidden layer (logistic regression). In addition, faster optimization was achieved by lesion classification models using ReLU as an activation function of hidden layers (Models 3 to 6) than the model using sigmoid as the activation function (Model 2). A comparison of Xavier and He normal initializations did not indicate significant differences in performance in terms of the optimization speed, and the Adam optimizer allows for faster optimization than the gradient descent optimizer. In contrast, in the case of Model 6, where the Adam optimizer and He normal initialization were employed together, the cost was emitted and the learning was not performed if iterations continued to be carried out. Among the 12 scenarios consisting of six lesion classification models and two unit sizes in datasets, the scenario with the highest accuracy uses a dataset with a unit size of 128×128 pixels and Model 5 (3-layered neural network with ReLU activation function, Xavier initialization, and Adam optimization), with a calculated accuracy of 0.975 (= 97.5%). We classified photothrombotic lesions and normal tissue areas using the classifier with the highest accuracy (a unit size of 128×128 pixels and Model 5 (3-layered neural network with ReLU activation function, Xavier initialization, and Adam optimization)) on four tested datasets, as shown in Figs. 4(a)–4(d). The results are shown in Figs. 4(e)–4(h). When the overall histological image and classification results were overlapped, as shown in Fig. 4(i), it was confirmed that the area in which photothrombotic brain damage occurred was well marked with high accuracy.

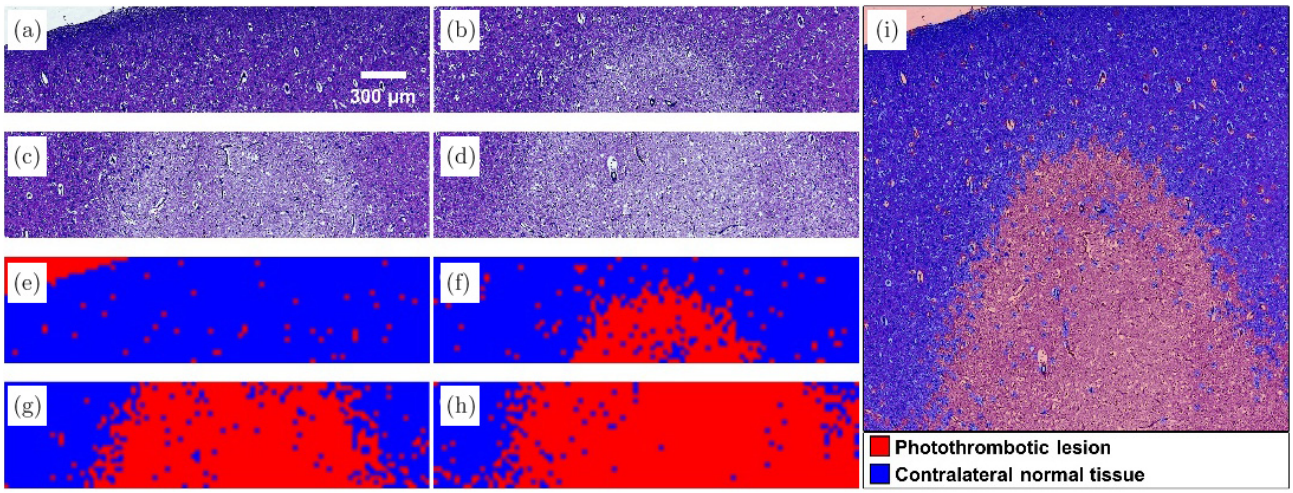

Fig. 4. (Color online) Classification of photothrombotic lesion and normal tissue areas using the classifier with the highest accuracy (a unit size of 128 × 128 pixels and Model 5 (3-layered neural network with ReLU activation function, Xavier initialization, and Adam optimization), accuracy = 0.975) on (a)–(d) four test datasets. (e)–(h) Results of classification of brain damage in each histological brain image, marked in red for photothrombotic lesion and blue for normal tissue. (i) Overlapped figure of the overall histological images and classification results.

3.3. *Discussion*

In this study, we established a machine learning algorithm that identifies damaged regions from histological images of rabbit brains where photothrombosis was induced. The machine learning-based lesion classification model (3-layered neural network with ReLU activation function, Xavier initialization, and Adam optimization with a unit size of 128 × 128 pixels in datasets) was obtained by comparing classification models under different conditions. A multilayered neural network including hidden layers and a ReLU activation function provides a more efficient learning rate and higher accuracy compared to a logistic regression with a single layer and sigmoid activation function. In general, He normal initialization is known to be better suited for neural networks using ReLU as an activation function in hidden layers than Xavier initialization; however, in this study, the two initializations showed no significant differences in learning efficiency and accuracy. (Models 3 (Xavier) and 4 (He normal) yielded accuracies of 0.965 and 0.968, respectively, when datasets with a unit size of 128 × 128 pixels were employed.) If iteration was sufficiently achieved, we confirmed that both gradient descent and Adam optimizer can optimize the lesion classification model to have an accuracy of 0.9 or higher in this study, except for the condition in Model 6.

For practical applications of machine learning-based lesion classification models to histopathological images, additional performance improvements and data processing are required. Methods to improve accuracy and learning rates in the lesion classification model include using neural networks with improved structures, such as a convolutional neural network (CNN)[29–31] and a recurrent neural network,[32–34] and using improved optimizers. In addition, differences in the components of light sources, photodetectors, and other optical components in microscopes and slide scanners can cause differences in colormaps, brightness, and background intensities. Models that are not optimized for these differences can provide false results. Therefore, the application of the lesion classification model using other microscopes requires retraining the model or establishing datasets with standardized brightness and colormap complementation. Furthermore, studies that apply SoftMax regression to classify multiple categories of brain tissues rather than the binary classification (normal/photothrombotic lesion) are likely to be useful not only in this context but also in other medical diagnostic techniques, such as pathologic classification of carcinoma grades.

4. Conclusion

A machine learning-based photothrombotic lesion classification model was established to identify lesions in histopathological rabbit brain images. We compared six lesion classification models with two

unit sizes of segmented images from the training and test datasets. The model consisting of a 3-layered neural network with a ReLU activation function, Xavier initialization, and Adam optimization, provided the highest accuracy (0.975) with a unit size of 128×128 pixels. We expect that the results of the development of machine learning-based classification algorithms and accuracy comparison will help in research on implementations of machine learning-based image processing and analysis in biomedical applications.

Conflicts of Interest

The authors declare that there is no conflicts of interest relevant to this article.

Acknowledgments

This research was supported by grants from the Korea Health Technology R&D Project through the Korea Health Industry Development Institute (KHIDI) funded by the Ministry of Health & Welfare (HI17C1501) and from Basic Science Research Program through the National Research Foundation of Korea (NRF) funded by the Ministry of Science & ICT (NRF-2020R1C1C1012230). S. H. Cho was supported by the semester internship program between Daegu Catholic University and Daegu-Gyeongbuk Medical Innovation Foundation. The authors would like to thank Prof. Young-Soo Sohn at the School of Biomedical Engineering of Daegu Catholic University for managing the semester internship program for conducting collaborative studies. Sang Hee Jo and Yoonhee Kim contributed equally to this work.

References

1. T. T. Mitchell, *Machine Learning* (McGraw Hill, United States of America, 1997).
2. J. Patel, S. Shah, P. Thakkar, K. Kotecha, "Predicting stock and stock price index movement using trend deterministic data preparation and machine learning techniques," *Expert Syst. Appl.* **42**, 259–268 (2015).
3. A. E. Maxwell, T. A. Warner, F. Fang, "Implementation of machine-learning classification in remote sensing: an applied review," *Int. J. Remote Sens.* **39**, 2784–2817 (2018).
4. P. Ma, J. Ma, X. Wang, L. Yang, N. Wang, "Deformable convolutional networks for multi-view 3D shape classification," *Electron. Lett.* **54**, 1373–1375 (2018).
5. A. Caggiano, J. Zhang, V. Alfieri, F. Caiazzo, R. Gao, R. Teti, "Machine learning-based image processing for on-line defect recognition in additive manufacturing," *CIRP Ann.* **68**, 451–454 (2019).
6. H. Ma, T. Celik, "FER-Net: Facial expression recognition using densely connected convolutional network," *Electron. Lett.* **55**, 184–186 (2019).
7. T. B. Alakus, I. Turkoglu, "Emotion recognition with deep learning using GAMEEMO data set," *Electron. Lett.* **56**, 1364–1367 (2020).
8. H. Zhang, C.-L. Hung, M. Liu, X. Hu, Y.-Y. Lin, "NCNet: Deep learning network models for predicting function of non-coding DNA," *Front. Genet.* **10**, 432 (2019).
9. G. Mata, M. Radojević, C. Fernandez-Lozano, I. Smal, N. Werij, M. Morales, E. Meijering, J. Rubio, "Automated neuron detection in high-content fluorescence microscopy images using machine learning," *Neuroinformatics* **17**, 253–269 (2019).
10. S. Ç Yetiş, A. Çapar, D. A. Ekinci, U. E. Ayten, B. E. Kerman, B. U. Töreyinb, "Myelin detection in fluorescence microscopy images using machine learning," *J. Neurosci. Methods* **346**, 108946 (2020).
11. Y. Rivenson, Z. Göröcs, H. Günaydin, Y. Zhang, H. Wang, A. Ozcan, "Deep learning microscopy," *Optica* **4**, 1437–1443 (2017).
12. H. Wang, Y. Rivenson, Y. Jin, Z. Wei, R. Gao, H. Günaydın, L. A. Bentolila, C. Kural, A. Ozcan, "Deep learning enables cross-modality super-resolution in fluorescence microscopy," *Nat. Methods* **16**, 103–110 (2019).
13. L. Fang, F. Monroe, S. W. Novak, L. Kirk, C. R. Schiavon, S. B. Yu, T. Zhang, M. Wu, K. Kastner, A. A. Latif, Z. Lin, A. Shaw, Y. Kubota, J. Mendenhall, Z. Zhang, G. Pekkurnaz, J. Mendenhall, K. Harris, J. Howard, U. Manor, "Deep learning-based point-scanning super-resolution imaging," *Nat. Methods* **18**, 406–416 (2021).
14. P. Lakhani, A. B. Prater, R. K. Hutson, K. P. Andriole, K. J. Dreyer, J. Morey, L. M. Prevedello, T. J. Clark, J. R. Geis, J. N. Itri, C. M. Hawkins, "Machine learning in radiology: applications beyond image interpretation," *J. Am. Coll. Radiol.* **15**, 350–359 (2018).
15. T. T. Tang, J. A. Zawaski, K. N. Francis, A. A. Qutub, M. W. Gaber, "Image-based classification of tumor type and growth rate using machine learning: a preclinical study," *Sci. Rep.* **9**, 12529 (2019).
16. A. Janowczyk, A. Madabhushi, "Deep learning for digital pathology image analysis: A comprehensive

tutorial with selected use cases," *J. Pathol. Inform.* **7**, 29 (2016).
17. T. Schlegl, P. Seeböck, S. M. Waldstein, U. Schmidt-Erfurth, G. Langs, Unsupervised anomaly detection with generative adversarial networks to guide marker discovery, *Int. Conf. on Information Processing in Medical Imaging*, pp. 146–157, Springer, Chem (2017).
18. A. Serag, A. Ion-Margineanu, H. Qureshi, R. McMillan, M. S. Martin, J. Diamond, P. O'Reilly, P. Hamilton, "Translational AI and deep learning in diagnostic pathology," *Front. Med.* **6**, 185 (2019).
19. Y. Zeng, J. Zhang, "A machine learning model for detecting invasive ductal carcinoma with Google Cloud AutoML Vision," *Compute. Biol. Med.* **122**, 103861 (2020).
20. T. Xia, A. Kumar, D. Feng, J. Kim, Patch-level tumor classification in digital histopathology images with domain adapted deep learning, *40th Annual Int. Conf. of the IEEE Engineering in Medicine and Biology Society (EMBC)*, pp. 644–647, IEEE (2018).
21. Y. Kim, Y. B. Lee, S. K. Bae, S. S. Oh, J. Choi, "Development of a photochemical thrombosis investigation system to obtain a rabbit ischemic stroke model," *Sci. Rep.* **11**, 5787 (2021).
22. D. R. Cox, "The regression analysis of binary sequences," *J. R. Stat. Soc. Series B* **20**, 215–232 (1958).
23. D. Jurafsky, J. Martin, "Logistic regression," *Speech and Language Processing*, Chap. 5, 3rd Edition, Draft, https://web.stanford.edu/∼jurafsky/slp3/5.pdf.
24. S. Kim, "Logistic (regression) classifier," https://docs.google.com/presentation/d/180ZISPNRV-WYKyV61xoZepZ_KVUK6mujIXuwXE0eKZuM/edit#slide=id.g1ed121957d_0_0.
25. X. Glorot, Y. Bengio, Understanding the difficulty of training deep feedforward neural networks, *Proc. 13th Int. Conf. on Artificial Intelligence and Statistics*, pp. 249–256, JMLR (2010).
26. K. He, X. Zhang, S. Ren, J. Sun, Delving deep into rectifiers: Surpassing human-level performance on imagenet classification, *Proc. IEEE Int. Conf. on Computer Vision*, pp. 1026–1034, IEEE, (2015).
27. D. P. Kingma, J. Ba, "Adam: A method for stochastic optimization," arXiv: 1412.6980.
28. Gradient Descent Optimization Algorithms Overview, http://shuuki4.github.io/deep%20learning/2016/05/20/Gradient-Descent-Algorithm-Overview.html.
29. F. F. Ting, Y. J. Tan, K. S. Sim, "Convolutional neural network improvement for breast cancer classification," *Expert Syst. Appl.* **120**, 103–115 (2019).
30. D. Mojahed, R. S. Ha, P. Chang, Y. Gan, X. Yao, B. Angelini, H. Hibshoosh, B. Taback, C. P. Hendon, "Fully automated postlumpectomy breast margin assessment utilizing convolutional neural network based optical coherence tomography image classification method," *Acad. Radiol.* **27**, e81–e86 (2020).
31. S. K. Khara, A. Nishad, A. Upadhyay, V. Bajaj, "Classification of emotions from EEG signals using time-order representation based on the S-transform and convolutional neural network," *Electron. Lett.* **56**, 1359–1361 (2020).
32. M. Gour, S. Jain, T. S. Kumar, "Residual learning based CNN for breast cancer histopathological image classification," *Int. J. Imag. Syst. Technol.* **30**, 621–635 (2020).
33. J. Lyu, X. Bi, S. H. Ling, "Multi-level cross residual network for lung nodule classification," *Sensors* **20**, 2837 (2020).
34. S. Liu, Q. Wang, G. Zhang, J. Du, B. Hu, Z. Zhang, "Using hyperspectral imaging automatic classification of gastric cancer grading with a shallow residual network," *Anal. Methods* **12**, 3844–3853 (2020).